

# Taming Mambas for Voxel Level 3D Medical Image Segmentation

Luca Lumetti\*  
Elisa Ficarra

Vittorio Pipoli\*  
Costantino Grana

Kevin Marchesini  
Federico Bolelli

University of Modena and Reggio Emilia, Italy

name.surname@unimore.it

## Abstract

Recently, the field of 3D medical segmentation has been dominated by deep learning models employing Convolutional Neural Networks (CNNs) and Transformer-based architectures, each with their distinctive strengths and limitations. CNNs are constrained by a local receptive field, whereas transformers are hindered by their substantial memory requirements as well as their data hungriness, making them not ideal for processing 3D medical volumes at a fine-grained level. For these reasons, fully convolutional neural networks, as nnU-Net, still dominate the scene when segmenting medical structures in 3D large medical volumes. Despite numerous advancements towards developing transformer variants with subquadratic time and memory complexity, these models still fall short in content-based reasoning. A recent breakthrough is Mamba, a Recurrent Neural Network (RNN) based on State Space Models (SSMs) outperforming Transformers in many long-context tasks (million-length sequences) on famous natural language processing and genomic benchmarks while keeping a linear complexity. In this paper, we evaluate the effectiveness of Mamba-based architectures in comparison to state-of-the-art convolutional and Transformer-based models for 3D medical image segmentation across three well-established datasets: Synapse Abdomen, MSD Brain Tumor, and ACDC. Additionally, we address the primary limitations of existing Mamba-based architectures by proposing alternative architectural designs, hence improving segmentation performances. The source code is publicly available to ensure reproducibility and facilitate further research. <sup>1</sup>

## 1. Introduction

Image segmentation is crucial in the analysis of medical images, typically serving as the preliminary step for

examining anatomical structures and surgical planning [2]. During the latest years Convolutional Neural Networks (CNN) [25] and in particular U-shaped Fully Convolutional Neural Networks (FCNN) have known wide adoption in the research community [31]. Despite their effectiveness, after the outbreak of vision transformers, FCNN has been replaced by hybrid architectures, made up by both Convolutional and Multi-Head Attention layers, aiming to mitigate the problem of local receptive field that characterizes the convolutional operation, relying on the transformer’s attention mechanism [36]. Several attempts have been made in the literature to integrate transformer-based architectures in the classic U-Net [7, 8, 12, 18, 19]. Even if these methods led to improvement in performances, it came at the cost of the quadratic memory footprint of the attention mechanism that alongside their data hungriness makes these approaches not ideal when applied to large 3D volumes.

In such regards, latest research put a lot of efforts in the reduction of the computational cost of the transformer architecture, proposing linear attention mechanism [3, 9, 38] and gating [34]. Anyway, most of them fall short when it comes to context modeling, in particular when the context-length is considerably high. Recently, the field of sequence modeling has been greatly influenced by an innovative architecture based on State-Space Model (SSM) [16] known as Mamba [14]. Mamba shown state-of-the-art capabilities in several Natural Language Processing (NLP) and genomic tasks improving the modeling of big context up to the order of a million tokens, making it a suitable candidate to efficiently process also 3D volumes, where the number of tokens reaches the same order of magnitude.

**Paper Contributions.** This paper aims to investigate the effectiveness of Mamba for 3D image segmentation by comparing state-of-the-art Mamba-based architectures with convolutional and Transformer-based segmentation models. Additionally, we seek to address the primary limitations of current Mamba-based architectures by proposing various strategies for integrating Mamba within a U-Net-based architecture. Specifically, we examine the impact of modeling

<sup>1</sup><https://anonymous.4open.science/r/WACV2025-TamingMamba/>

\*Equal contribution. Authors are allowed to list their name first in their CVs.

directionality on one or more axes and explore the use of Mamba as a selective copying mechanism in skip connections. To perform our experimental evaluation, we employ three different well known datasets, MSD BrainTumour [1], Synapse Multi-organ [24], and ACDC [4]. The code is publicly released to encourage further research.

## 2. Related Work

Convolutional Neural Networks (CNNs) [25] have been the dominant solution for both 2D and 3D medical image segmentation for years. Among these, U-Net [31], characterized by its U-shaped symmetric encoder-decoder structure with skip connections, represents an effective architecture that subsequent models have continued to adopt until the present day. Following U-Net, several variants have been introduced, including Res-U-Net [10], Dense-U-Net [6], V-Net [29], 3D U-Net and its state-of-the-art ecosystem nnU-Net [22], each proposing enhancements to the original framework. Despite their advancements, CNNs inherently face limitations in capturing global patterns due to the locality of the convolutional operator. In response, significant research efforts have been directed towards integrating the attention mechanisms of transformers [36] with U-Net-based architectures. This integration aims to leverage both local and global dependencies, as evidenced by models such as MedFormer [12], TransUNet [8], Swin-UNet [7], UNETR [19], and Swin-UNETR [18]. However, the attention mechanism’s quadratic complexity forces the imposition of constraints, such as window-based or axial-based attention, to mitigate computational demands. While various studies have attempted to reduce this complexity [3, 9, 23, 38], none have matched the performance of traditional attention mechanisms in long-context modeling.

Recent developments have introduced a novel architecture, Mamba [14], predicated on state space modeling [16, 17], which promises capabilities for long-context content-based reasoning with linear-time complexity. Mamba has demonstrated superior performance over state-of-the-art transformer models, such as Pythia-6.9B [5], GPT-J-6B [37], OPT-6.7B [45], Hyena [30], in tasks requiring long-context content-based reasoning, such as natural language processing and genomic analyses, with inputs of up to million-length scales.

Due to their effectiveness and versatility, Mamba-based architectures have been rapidly adapted to various domains, including Computer Vision [26]. In addition, given that segmenting 3D volumes can be seen as processing sequences composed of millions of voxels, several researchers have devoted significant efforts to adapting the Mamba architecture for both 2D and 3D segmentation, yielding promising results [13, 33, 40, 42, 44]. Among the various contributions, UMamba remains one of the most significant in the field given the model ability to adapt effectively to new datasets

without the need for extensive hyperparameter tuning. In particular, in their work the authors propose two architectures, namely UMambaEnc and UMambaBot, both inheriting their core structure from U-Net and harnessing Mamba-based layers. The former integrates the Mamba-layers in the encoder part of the architecture, while the latter integrates a single Mamba-layer in the bottleneck. Despite their effectiveness, authors did not focus on the *directionality problem* that derives from employing a recurrent network to extract patterns from data that has more than one spatial dimension. Indeed, once a 3D volume is flattened into a sequence, each voxel is assigned a position within the sequence. This results in the model being able to analyze the latter elements of the sequence by leveraging information from the preceding part. However, it lacks contextual information when processing the initial part of the sequence.

The aforementioned advancements in the field motivated us to devise Mamba architectures for 3D image segmentation, paying particular attention to the directionality.

## 3. Method

In this section, all the theoretical concepts related to the vanilla Mamba architecture (a set of stacked Mamba blocks) are introduced. Then, we thoroughly explain how Mamba blocks can be employed to extract patterns from 3D volumes and illustrate approaches to integrate such blocks into a U-Net architecture for 3D medical imaging segmentation.

### 3.1. Preliminaries

**State Space Models.** A State-Space Model (SSM) is a mathematical representation of a dynamic system which maps a 1D input  $x(t) \in \mathbb{R}$  to a  $ND$  latent state  $h(t) \in \mathbb{R}^N$  before projecting it to a 1D output signal  $y(t) \in \mathbb{R}$ . This system uses  $A \in \mathbb{R}^{N \times N}$  as the evolution parameter,  $B \in \mathbb{R}^{N \times 1}$ , and  $C \in \mathbb{R}^{1 \times N}$  as the projection parameters:

$$h'(t) = Ah(t) + Bx(t) \quad (1)$$

$$y(t) = Ch(t) \quad (2)$$

Together, the previous equations aim to predict the state of a system from observed data. Since the input is expected to be continuous, the main representation of the SSM is a continuous-time representation.

To employ Eq. (2) in a real-world scenario, and more specifically into a neural network, a discretization of the variable  $t$  is required and can be achieved by introducing a step-size parameter  $\Delta$  and a discretization rule, which in this case is the *zero-order hold*:

$$\bar{A} = \exp(\Delta A) \quad (3)$$

$$\bar{B} = (\Delta A)^{-1}(\exp(\Delta A) - I)\Delta B \quad (4)$$

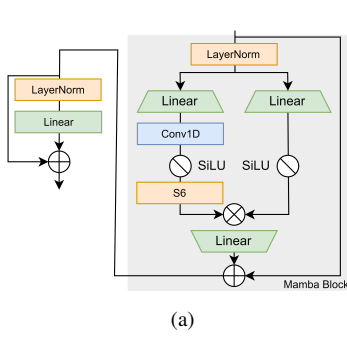


Figure 1. From left to right: (a) The unidirectional Mamba layer, which processes input sequences only in the forward direction. The layers within the gray square collectively form the Mamba Block. (b) The bidirectional Mamba layer, consisting of two unidirectional Mamba layers: the left branch processes the forward sequences, while the right branch processes the reversed sequences.

This yield to the following discrete state space model that can be computed in a recurrent fashion:

$$h_{t+1} = \bar{A}h_t + \bar{B}x_t \quad (5)$$

$$y_t = Ch_t \quad (6)$$

This basic SSM performs very poorly in practice due to gradients scaling exponentially in the sequence length. To address this issue, Mamba propose two key elements: imposing a structure to the matrix  $A$ , using the HiPPO theory [15], and including a selection mechanism, i.e., making the parameters  $B$ ,  $C$ , and  $\Delta$  input-dependent through a linear projection:

$$\begin{aligned} B &= \text{Linear}_N(x) \\ C &= \text{Linear}_N(x) \\ \Delta &= \text{SoftPlus}(\text{Parameter} + \text{Broadcast}_D(\text{Linear}_1(x))) \end{aligned} \quad (7)$$

This formulation, together with an efficient implementation of the process by means of a selective scan algorithm that allows the model to filter out irrelevant information, constitutes the so called **S6** model [14]. To construct a Mamba block, an initial linear projection is employed to expand the input tokens embeddings. Then, a convolution before S6 is applied to prevent independent input token calculations and finally the SSM output is projected back to the original dimension together with a skip connection. SiLU non-linearities are employed [20]. A visual representation of this block is depicted in gray within Fig. 1. We refer to the the original publication [14] for an in-depth understanding of the discussed methodology.

### 3.2. Vision Mamba

Mamba is a sequence to sequence model, thus only able to handle 1D sequences. In order to apply it to 2D images and 3D volumes, a 1D sequence flattenization of

pixel (or voxels) is required. Differently from the approach adopted in Vision Transformer, where the quadratic cost of self-attention with respect to the number of pixel prevent their scaling to “realistic” input size and requires to extract patches to reduce the input spatial dimension, Mamba allows us a linear-time sequence modelling of the input, preventing any sampling. Patch down-sampling is a major issue in medical image segmentation, due to the need for voxel-wise details, which is usually enforced by the large medical input data.

One downside of Mamba is that it is not permutation-invariant. In contrast to the transformer self-attention mechanism, where each token can gather information from every other token in the sequence, Mamba restricts each token to only infer information from the current state, resulting in an approximation of the past tokens only. This means that when Mamba is employed for image segmentation tasks, the very first pixels (or voxels) in the sequence do not have any context awareness. For this reason, instead of directly including the Mamba Block into our U-Net architecture, by taking inspiration from the ViT architecture [11] we developed a wrapper. The wrapping, consisting of an additional LayerNorm and an MLP head followed by a skip connection, allows us to improve Mamba stability. We denote this module as the Mamba Layer, illustrated in Fig. 1a. Subsequently, we integrated two instances of the Mamba Layer into a unified module. This module, named Bidirectional 3D Mamba Layer, takes as input a 3D volume with dimensions  $(B, H, W, D, C)$ . It flattens the spatial dimensions and manages the sequence bidirectionally by feeding one of the two layers with the sequence in the backward direction. Subsequently, the output from this layer is reversed to its original order and then summed token by token with the output of the “straight” layer. Finally, the sum is normalized and reshaped back into a 3D volume. This layer is depicted in Fig. 1b.

In the following, the strategies we introduce to integrate the Mamba Layer into nnU-Net are detailed. Fig. 2 depicts our U-Net architectures enriched with Mamba layers.

**SegMamba.** The initially proposed integration involves the inclusion of a singular (unidirectional) Mamba Layer preceding each pooling convolution and the bottleneck of U-Net. This strategic placement is designed to enhance the overall contextual understanding, addressing the inherent limitations in global context that convolutions often encounter, while limiting the additional number of parameters.

**SegMambaSkip.** One of the universally recognized strength points of the U-Net architecture lies in its skipped connections [31], which allow the decoding part of the network to access fine-grained details coming from the encoder. Meanwhile, Mamba has been devised to efficiently select data in an input-dependent manner, thus being capable of filtering out irrelevant information and remembering

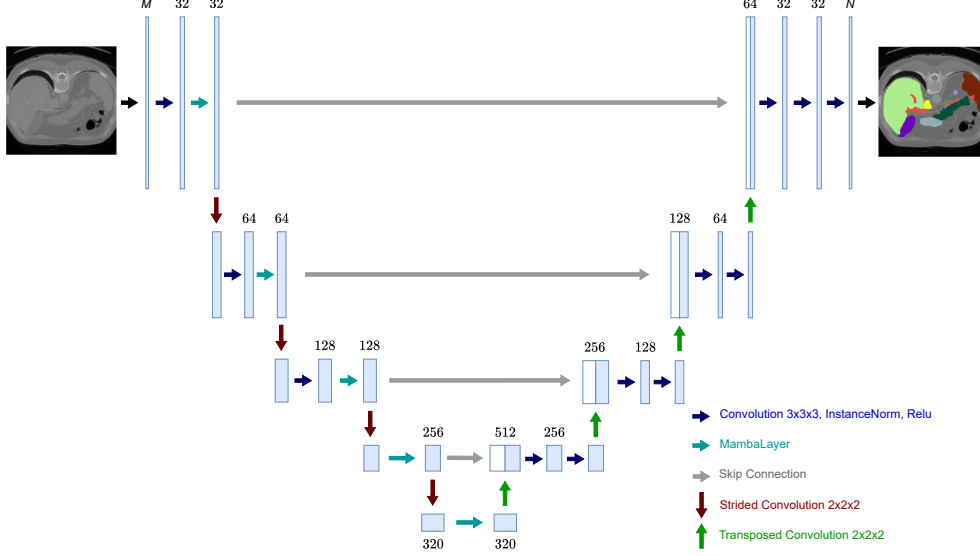


Figure 2. U-Net architecture integrating our proposed Mamba Layers. By properly selecting the Mamba Layers (turquoise arrows), SegMamba, BiSegMamba, and MultiSegMamba are obtained. To obtain SegMambaSkip the currently displayed Mamba Layers (turquoise arrows) must be replaced by the standard U-Net convolution (blue arrow) and corresponding Mamba Layers must be placed within the skip connections (gray arrows).

relevant ones. Hence, we augment the skip connections in the U-Net architecture by inserting an additional Bidirectional 3D Mamba Layer before concatenating the activation map to the corresponding decoder output.

**BiSegMamba.** It includes our Bidirectional 3D Mamba Layer before each downsampling step as well as in the U-Net bottleneck. By leveraging both directions of a single sequential arrangement in BiSegMamba, we strike a balance between computational efficiency and model effectiveness. The Bidirectional 3D Mamba Layer enables the model to effectively weigh the importance of tokens across various spatial dimensions, without the need to consider all possible permutations. This approach is particularly beneficial when dealing with distant dependencies and selective information processing, enhancing the ability to discern relevant features during downsampling and in bottleneck layers.

**MultiSegMamba.** The order of input tokens is important within Mamba. For this reason, we propose to process all conceivable sequential arrangements of the volume, resulting in a total of six possible permutations for the three spatial dimensions ( $H$ ,  $W$ ,  $D$ ) of a 3D volume. This yields a total of 12 distinct sequences, accounting for both the forward and backward directions of the six permutations. The rationale behind seeking multiple directions stems from the necessity for each voxel to exploit spatial information in all conceivable orientations. If we were to consider only a single sequence, such as  $(H, W, D).flatten()$ , the distance between the first token at index  $(0, 0, 0)$  and the token at index  $(0, 0, 1)$  would be  $H * W$  instead of 1. Typically, the values of  $H$  and  $W$  are in the order of

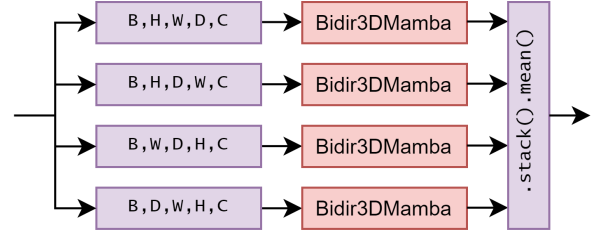


Figure 3. To achieve multi-directionality, four Bidirectional 3D Mamba Layers are employed, corresponding to four out of the six possible permutations of the triplet  $(H, W, D)$ . The outputs of each layer is stacked, and the mean per token is computed.

$10^2$ , resulting in a total distance of  $10^4$ . Due to memory constraints, we only encompass 4 out of 6 possible directions.<sup>2</sup> By incorporating multiple directions, we maintain linear complexity while affording each token superior spatial awareness. This approach ensures that neighboring tokens are indeed proximate in the obtained representation, enhancing the overall spatial awareness of the model. To aggregate the output sequences of all the modules involved, we stack each sequence on a new axis and compute the mean value across it (Fig. 3). This module substitute the Bidirectional 3D Mamba Layer in BiSegMamba.

### 3.3. Implementation Details

Details regarding patch shape, batch size, and other pipeline settings are reported in Tab. 1. All of our models have been trained for 300 epochs using RAdam, a learning rate of 0.0003 and a linear learning rate scheduler. For

<sup>2</sup>We use  $(H, W, D)$ ,  $(H, D, W)$ ,  $(W, H, D)$ , and  $(D, W, H)$ .



Table 1. Configuration of the proposed models when trained on the selected datasets.

	BrainTumour	Synapse	ACDC
Spacing	[1, 1, 1]	[3, 0.76, 0.76]	[6.35, 1.52, 1.52]
Median shape	$138 \times 170 \times 138$	$148 \times 512 \times 512$	$13 \times 246 \times 213$
Crop size	$128 \times 128 \times 128$	$48 \times 192 \times 192$	$14 \times 256 \times 224$
Batch size	2	2	4

the parameters initialization of the Mamba layers, we scale the weights of residual layers at initialization by a factor of  $1/\sqrt{N}$  where  $N$  is the number of residual layers. This is the same as in GPT-2 paper and employed in the Mamba source code. The inner dimension of the State Space Model (i.e., the size of the evolution parameter  $A$ , Sec. 3.1) is defined as  $\min(C, 256)$  where  $C$  is the number of token’s channels in the input sequence. Training has been performed on an A100 Nvidia GPU using CUDA 11.8 and PyTorch 2.1.2.

## 4. Experiments and Results

**Datasets.** We conducted experiments using three different well known datasets: MSD BrainTumour [1], Synapse Multi-organ [24], and ACDC [4]. It is worth noticing that the selected experimental setting aligns with the existing literature on medical image segmentation [7, 19, 35, 41, 43, 46]

*MSD BrainTumour.* The first one is the BrainTumour segmentation dataset from the Medical Segmentation Decathlon (MSD BrainTumour) [1]. It consists of 484 MRI images, each containing four channels: FLAIR, T1w, T1gd, and T2w. The images were annotated with three tumour sub-regions: edema (ED), enhancing tumour (ET), and non-enhancing tumour (NET). To be coherent with the results reported by [19], the segmentation metrics were computed on the classes ET, tumour core (TC, which is the union of ET and NET), and whole tumour (WT, which is the union of ED, ET and NET). Following the split provided by [19], we employed 95% of the dataset as a training/validation set with 5-fold cross-validation, and 5% for testing purposes.

*Synapse Multi-organ.* The second dataset is the Synapse Multi-organ segmentation dataset [24], published within the MICCAI 2015 Multi-Atlas Abdomen Labeling Challenge. This dataset includes 3 779 axial contrast-enhanced abdominal CT images from 30 abdominal CT scans, with each volume consisting of 85 to 198 slices. We adopted the same split as in [8], with 18 cases for training and 12 cases for testing. In line with our competitors, the evaluation metrics for this dataset were calculated for eight out of thirteen annotated abdominal organs: aorta, gallbladder, left kidney, right kidney, liver, pancreas, spleen and stomach.

*ACDC.* Lastly, the third dataset employed is the ACDC dataset [4]. It comprises 100 MRI scans, each labeled for the left ventricle (LV), right ventricle (RV), and myocardium (Myo). We divided this dataset into 80 samples

for training and validation, and 20 test samples, following the split described in [8].

**Evaluation Metrics.** We employ Dice Similarity Coefficient (DSC in %) and the 95th percentile Hausdorff Distance (HD95 in mm), two widely accepted metrics for segmentation task [28].

The DSC has practically the same meaning as the IoU (Intersection over Union), but the first one is better suited when the region of interest is much smaller than the background. In such a scenario, DSC can be more robust and informative than IoU since more weight is given to the correctly identified region. The DSC metric, and its relationship with the IoU, are expressed by the following formula:

$$\text{DSC}(P, GT) = \frac{2 \times |P \cap GT|}{|P| + |GT|} = \frac{2 \times \text{IoU}}{1 + \text{IoU}} \quad (8)$$

where  $P$  is the model prediction and  $GT$  is the ground truth.

On the other hand, the HD95 computes the maximum distance between two sets of points, considering the 95th percentile of these distances. In general, the 95th percentile of the distances between boundary points in  $A$  and  $B$  is defined as follows:

$$d_{95}(A, B) = x_{a \in A}^{95} \left\{ \min_{b \in B} d(a, b) \right\} \quad (9)$$

where  $x_{a \in A}^{95} \{ \}$  denotes the 95th percentile of the elements in the set enclosed within the brackets. Given the set formed by the pixels in the predicted mask ( $P$ ) and the set of pixels belonging to the ground truth ( $GT$ ), the Hausdorff distance is determined as the maximum value of the two distances between  $P$  and  $GT$  and  $GT$  and  $P$  at the 95th percentile:

$$\text{HD95}(P, GT) = \max \left\{ d_{95}(P, GT), d_{95}(GT, P) \right\} \quad (10)$$

By using the 95th percentile, this metric provides a robust evaluation that is less sensitive to outliers or extreme differences between the sets of points.

**Compared Methods.** Performance comparison has been performed on recently proposed methods for medical image segmentation. Specifically, considered competitors can be classified into three main groups: CNN-, Transformer-, and Mamba-based architectures.

In the former group, we include the original nnU-Net [22] configuration making use of the vanilla U-Net architecture (nnU-Net), and its variations based on the U-Net with residual connections in the encoder (nnU-Net ResEnc). Furthermore, the transformer-inspired-CNN-modification based on ConvNeXt blocks, MedNeXt [32], has been considered in its two variations K3, and K5. For what concerns Transformer-based architectures, we compare our proposals with TransU-Net [8], TransBTS [39], CoTr [41],

Table 2. 5-fold cross-validation results on the BrainTumor dataset. Our proposals are marked with †. Standard deviations for the average scores over the 5 folds are reported. Best results are in **bold** while the second best are underlined.

	Model	Average		WT		ET		TC	
		HD95↓	DSC↑	HD95↓	DSC↑	HD95↓	DSC↑	HD95↓	DSC↑
CNNs	nnU-Net [22]	4.53±0.17	85.74±0.93	4.21	91.15	3.89	80.76	5.47	85.29
	nnU-Net ResEnc [22]	4.12±0.16	85.60±0.70	3.71	89.93	<u>3.72</u>	80.86	4.93	86.01
	MedNeXt-M-K3 [32]	6.35±0.21	85.27±0.45	4.59	90.84	6.57	<u>80.88</u>	7.89	84.10
	MedNeXt-M-K5 [32]	6.67±0.30	84.79±0.81	4.93	88.93	6.75	79.97	8.33	85.47
Transformers	TransU-Net [8]	13.18±0.83	64.14±0.84	14.42	70.16	10.80	54.31	14.31	67.94
	TransBTS [39]	9.83±0.22	69.72±0.56	10.32	78.22	10.20	57.26	8.97	73.68
	CoTr [41]	9.96±0.19	68.21±0.42	9.25	74.81	9.58	55.14	11.04	74.67
	UNETR [19]	9.04±0.41	70.92±1.02	8.03	78.85	9.83	58.06	9.25	75.85
	SwinU-Net [7]	9.98±0.33	67.95±0.57	8.85	76.43	10.31	57.21	10.77	70.20
	Swin-UNETR [18]	6.77±0.25	84.07±0.67	7.13	88.92	7.54	79.93	5.63	83.34
	LeViT-UNet-384s [43]	8.56±0.30	70.06±0.87	8.20	77.06	8.60	58.10	8.89	75.03
	MISSFormer [21]	9.21±0.19	83.08±0.39	8.40	88.21	9.57	79.71	9.64	81.33
	nnFormer [46]	4.05±0.25	86.34±0.51	<u>3.47</u>	91.28	4.24	<b>81.76</b>	4.46	85.97
Mamba	UMambaBot [27]	<b>3.80±0.22</b>	86.35±0.77	3.49	92.10	3.80	80.04	4.10	86.90
	UMambaEnc [27]	4.17±0.18	86.16±0.53	3.63	92.30	4.44	79.72	4.43	86.46
	SegMambaSkip†	4.53±0.20	85.25±0.81	3.61	92.11	5.43	78.85	4.54	84.79
	SegMamba†	<u>3.82±0.11</u>	<u>86.66±0.45</u>	3.66	92.26	3.83	80.77	<u>3.96</u>	<u>86.96</u>
	BiSegMamba†	3.85±0.16	85.75±0.60	<b>3.38</b>	<b>92.43</b>	<b>3.46</b>	79.60	4.70	85.21
	MultiSegMamba†	3.84±0.24	<b>86.70±0.51</b>	3.72	92.09	3.88	80.84	<b>3.93</b>	<b>87.18</b>

Table 3. 5-fold cross-validation results on the Synapse Abdomen dataset. Our proposals are marked with †. For space constraints, single class results only report the Dice score. Standard deviations for the average scores over the 5 folds are reported. Best results are in **bold** while the second best are underlined.

	Model	Average		Aorta	Gallb.	L.Kidn.	R.Kidn.	Liver	Pancr.	Spleen	Stom.
		HD95↓	DSC↑								
CNNs	nnU-Net [22]	10.91±0.69	86.21±1.19	91.65	70.01	86.67	85.75	96.11	83.22	90.69	85.55
	nnU-Net ResEnc [22]	7.70±0.42	86.61±1.07	89.94	64.20	90.79	91.18	<b>97.36</b>	79.48	92.03	<b>87.93</b>
	MedNeXt-M-K3 [32]	18.99±0.53	85.70±0.77	<u>92.44</u>	<b>72.75</b>	87.62	86.21	<u>97.15</u>	81.17	90.3	77.93
	MedNeXt-M-K5 [32]	17.30±0.60	86.00±0.86	92.15	71.66	87.89	87.43	96.91	80.26	90.95	80.78
Transformers	TransU-Net [8]	32.27±1.01	77.24±0.91	86.88	62.59	81.35	76.98	94.45	55.57	84.97	75.12
	TransBTS [39]	11.98±0.67	83.27±1.06	91.95	62.24	86.91	87.15	96.67	71.91	91.62	77.70
	CoTr [41]	9.35±0.39	84.67±0.75	<b>92.77</b>	63.07	87.98	86.84	92.75	78.63	94.54	80.76
	UNETR [19]	19.15±0.84	78.10±1.12	89.75	55.81	85.71	84.71	94.00	60.23	84.47	70.14
	SwinU-Net [7]	22.02±0.70	79.06±0.73	85.65	66.46	83.03	79.37	94.02	56.57	90.67	76.72
	Swin-UNETR [18]	11.02±0.72	83.64±1.31	91.22	66.48	87.09	86.62	95.99	68.79	95.72	77.19
	LeViT-UNet-384s [43]	16.80±0.81	78.38±0.99	87.52	61.77	84.04	79.87	92.8	59.20	88.84	73.03
	MISSFormer [21]	18.50±0.59	81.87±0.85	86.48	68.92	85.56	81.60	94.24	65.44	91.7	80.99
	nnFormer [46]	11.14±0.48	86.56±0.64	91.63	69.85	86.61	86.55	96.97	<b>83.68</b>	90.72	86.44
Mamba	UMambaBot [27]	7.35±0.42	86.88±0.80	89.88	60.14	89.99	94.37	96.81	82.33	95.66	85.88
	UMambaEnc [27]	7.83±0.50	87.82±0.75	89.57	65.20	89.46	94.84	96.97	83.35	<b>96.80</b>	86.40
	SegMambaSkip†	6.29±0.47	88.26±0.89	89.64	69.04	93.40	94.91	<b>96.80</b>	79.61	<u>96.45</u>	86.19
	SegMamba†	7.91±0.38	87.48±0.77	89.59	62.21	<u>93.65</u>	94.81	96.82	80.72	95.22	86.85
	BiSegMamba†	<u>5.99±0.53</u>	<u>88.29±0.90</u>	91.02	70.12	<u>92.98</u>	94.32	96.94	79.08	96.26	85.58
	MultiSegMamba†	<b>5.98±0.36</b>	<b>88.93±0.84</b>	91.36	71.78	<b>94.00</b>	<u>94.88</u>	95.76	80.65	96.22	86.77

an hybrid architecture combining convolutional and transformer modules, UNETR [19], SwinU-Net [7] and its UNETR-based variation Swin-UNETR [18], LeViT-UNet-384s [43], MISSFormer [21], and the recently published nnFormer [46]. Finally, we include UMamba [27] in its two variations UMambaBot and UMambaEnc.

In our experiments, a standardized scheme for hyperpa-

rameter configuration has been adopted. Whenever available, the self-configuration method capabilities have been employed, otherwise, we opted for the default configuration (if any) or the one closest to the respective dataset, reducing the learning rate until convergence. Models are trained from scratch without any pre-training data. The nnU-Net five-fold cross-validation schema has always been employed.

Table 4. 5-fold cross-validation results on the Automatic Cardiac Diagnosis (ACDC) dataset. Our proposals are marked with †. The evaluation metric is the DSC (%). Best results are in bold while second best are underlined.

	Model	Average	RV	Myo	LV
CNNs	nnU-Net [22]	91.42	90.1	88.74	95.41
	nnU-Net ResEnc [22]	90.84	89.17	88.52	94.84
	MedNeXt-M-K3 [32]	91.64	89.43	<u>89.77</u>	95.72
	MedNeXt-M-K5 [32]	90.70	88.5	88.88	94.73
Transformers	TransUNet [8]	89.75	88.88	84.66	95.7
	TransBTS [39]	91.29	90.42	87.94	95.51
	CoTr [41]	90.90	89.17	88.34	95.18
	UNETR [19]	88.72	85.55	86.48	94.12
	SwinU-Net [7]	89.97	88.29	85.61	<b>96.01</b>
	Swin-UNETR [18]	91.36	90.48	87.84	<u>95.75</u>
	LeViT-UNet-384s [43]	90.21	89.78	87.10	<u>93.75</u>
	MISSFormer [21]	87.73	86.55	85.24	91.42
	nnFormer [46]	<u>91.87</u>	<b>90.78</b>	89.37	95.46
Mamba	UMambaBot [27]	90.44	87.67	88.76	94.89
	UMambaEnc [27]	90.07	87.34	88.23	94.65
	SegMambaSkip†	91.49	89.58	89.51	95.39
	SegMamba†	91.33	89.37	89.40	95.22
	BiSegMamba†	91.50	89.46	89.66	95.37
	MultiSegMamba†	<b>92.04</b>	90.39	<b>90.29</b>	95.44

Table 5. Computational comparison on the Synapse dataset. Our proposals are marked with †. The number of parameters is expressed in millions [M] and VRAM in gigabyte [GB]. Training and inference times, expressed in hours [h] and seconds [s], respectively, are obtained on an Nvidia A100 with 80GB of memory. All competitor models were trained for 1000 epochs, as recommended by most of their original papers, while our method achieved convergence in only 300 epochs. Inference times is the average across all test volumes.

	Models	Params	GFLOPs	VRAM	Tr.	Inf.
CNNs	nnU-Net [22]	30.64	410.11	7.65	9.2	21.80
	nnU-Net ResEnc [22]	57.50	502.49	10.00	10.0	22.20
	MedNeXt-M-K3 [32]	32.65	248.03	15.32	67.6	153.60
	MedNeXt-M-K5 [32]	34.75	308.01	18.85	218.3	416.90
Transf.	TransUNet [8]	96.07	88.91	16.25	26.5	73.90
	CoTr [41]	50.12	369.22	8.10	18.6	41.40
	UNETR [19]	92.49	75.76	15.29	15.4	39.50
	Swin-UNETR [18]	62.83	384.20	13.91	22.0	38.70
	nnFormer [46]	150.50	213.41	9.73	8.2	20.60
Mamba	UMambaBot [27]	41.95	156.32	13.55	22.0	54.20
	UMambaEnc [27]	42.85	231.18	26.42	37.9	89.30
	SegMambaSkip†	62.36	486.92	29.26	12.6	93.50
	SegMamba†	61.49	480.90	25.61	12.7	99.60
	BiSegMamba†	64.75	494.17	27.31	16.5	134.10
	MultiSegMamba†	68.46	527.56	36.92	18.2	149.00

**Results.** As shown in Tab. 2, Tab. 3, and Tab. 4 our proposed models consistently outperform all competing approaches, demonstrating superior overall performance across all the considered datasets. In general, BiSegMamba, and MultiSegMamba consistently outperform SegMambaSkip, even if the latter is always competitive with

state-of-the-art models and on some specific classes proves to be superior to all.

As the results on the BrainTumor dataset (Table 2) show, SegMamba, BiSegMamba, and MultiSegMamba always outperform SegMambaSkip on average metrics and on most individual classes taken separately. Among the SegMamba models, MultiSegMamba, the one that harnesses more directions, outperforms the other configurations, demonstrating the importance of modeling multiple directions. Excluding nnFormer, our Mamba-based architectures gain more than 3 dice points over best performing transformer-based architectures and up to 1 dice point over nnU-Net.

For what concerns the Synapse Abdomen dataset (Table 3), characterized by a larger number of classes, results show that our model showcase substantial improvements in kidney and spleen segmentation, as well as on average HD95 and DSC, when compared to state-of-the-art architectures. Remarkably, the inclusion of four distinct directions yields a more pronounced improvement on gallbladder segmentation, which is the most difficult to segment. Indeed, the gallbladder is significantly smaller and varies more in shape and position compared to other organs such as the liver, which is larger and more consistently shaped. Moreover, the close proximity of gallbladder to other organs and structures in the abdominal cavity increases the complexity of distinguishing it in medical images. Results on gallbladder segmentation show that SegMamba reaches 62.21 Dice points, while its multidirection versions such as BiSegMamba and MultiSegMamba improve over it by 8 and 10 points respectively.

Finally, results on the ACDC dataset are presented in Table 4. This table highlights that MultiSegMamba outperforms all its variants that model less directions, and that MultiSegMamba and BiSegMamba consistently outperform SegMambaSkip and all the U-Mamba variations.

**About Model Size.** In Table 5 a comprehensive computational comparison on the Synapse dataset is reported considering the number of parameters (millions), GFLOPs, and GPU memory. Our proposed models have a higher number of parameters compared to classical CNN approaches, while being comparable to or often having fewer parameters than transformer-based models. More specifically, the number of parameters of our models (~60M) are, on average, the double with respect to nnU-Net (~31M), comparable to those of nnU-Net ResEnc (~57M), and much lower than those of transformer-based models (from ~95M of TransUNet and UNETR, up to 150M of nnFormer).

**Qualitative Evaluation.** Fig. 4 depicts a qualitative comparison of the four variations of the proposed architecture. The comparison is performed on samples taken from the Synapse Abdomen evaluation set. As can be seen, all of our Mamba-based variations perform qualitatively similarly, but the ones leveraging multiple directions are less

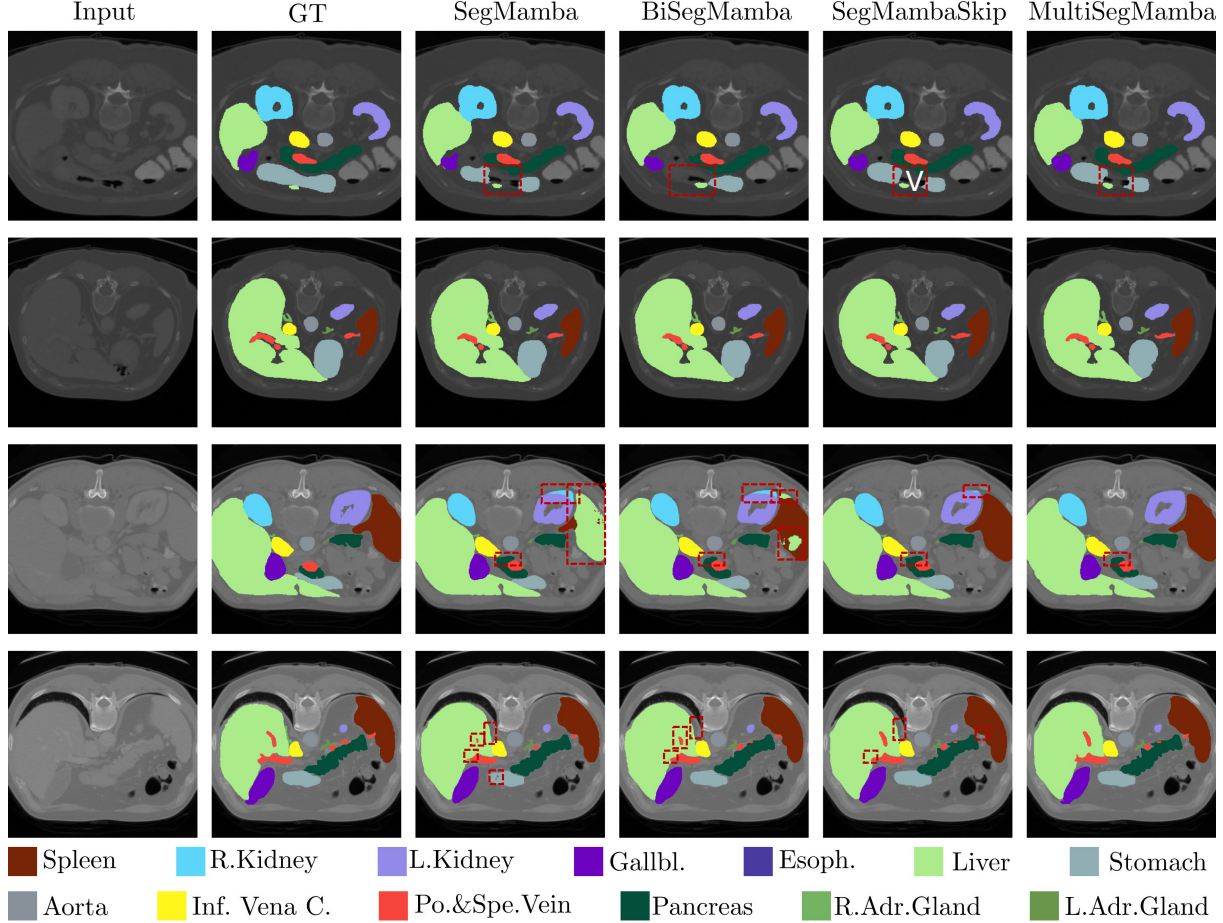


Figure 4. Visualization of segmentation results for four sample cases from the Synapse Abdomen evaluation set. Annotation errors are marked with red dashed boxes. The figure is best viewed in color and zoomed in. From left to right: Input, Ground Truth (GT), SegMamba, BiSegMamba, SegMambaSkip, and MultiSegMamba.

prone to errors when dealing with fine-grained details. This confirms the quantitative results previously discussed.

## 5. Conclusion

This paper aims to assess the efficacy of the Mamba State Space Model for 3D medical image segmentation, comparing it with advanced convolutional and Transformer-based architectures. Additionally, we propose alternative designs for Mamba architectures to address their key limitations. Specifically, we integrate Mamba at various stages within the standard U-Net framework, either in skip connections or prior to pooling operations, utilizing both single-directional, bi-directional, and multi-directional implementations. The overall framework blends Convolutions and State Space Models, leveraging the former for encoding precise spatial information, while addressing the latter to model long-range voxel-level interactions. Mamba offer a dual advantage, providing a global context alongside voxel-wise precision, the former absent in traditional convolutional layers due to

limited receptive fields and the latter absent in Transformers due to their computational complexity.

Our experimental results highlight the substantial improvement in HD95 and DSC metrics on three well-known datasets compared to nnU-Net and different transformer-based networks. We showcase Mamba versatility by adapting it from its original use in text generation and large language models to achieve state-of-the-art results in a completely different task. This adaptability highlights Mamba potential beyond its initial design, demonstrating its efficacy on image encoding and segmentation.

**Limitations And Future Works.** Despite the advancements made with the Mamba model, two key limitations can be identified.

First, as Mamba is inherently a causal model, its application to non-causal visual data requires modification. Specifically, we tried to solve this problem by processing each sequence both forward and backward. Anyway, this introduces redundancy increasing the risk of overfitting. We believe that more efficient approaches could be developed to



address this issue.

Second, to capture spatial relationships, we unfold image patches from multiple directions, but more effective methods, such as identifying optimal scanning paths or partitioning larger volumes into smaller neighborhoods, may exist. Furthermore, employing too many directions can significantly increase computational demands and redundancy as mentioned before.

## References

- [1] Michela Antonelli, Annika Reinke, Spyridon Bakas, Keyvan Farahani, Annette Kopp-Schneider, Bennett A Landman, Geert Litjens, Bjoern Menze, Olaf Ronneberger, Ronald M Summers, et al. The Medical Segmentation Decathlon. *Nature Communications*, 13(1):4128, 2022. [2](#), [5](#)
- [2] Saeid Asgari Taghanaki, Kumar Abhishek, Joseph Paul Cohen, Julien Cohen-Adad, and Ghassan Hamarneh. Deep semantic segmentation of natural and medical images: a review. *Artificial Intelligence Review*, 54:137–178, 2021. [1](#)
- [3] Iz Beltagy, Matthew E Peters, and Arman Cohan. Longformer: The Long-Document Transformer. *arXiv preprint arXiv:2004.05150*, 2020. [1](#), [2](#)
- [4] Olivier Bernard, Alain Lalonde, Clement Zotti, Frederick Cervenansky, Xin Yang, Pheng-Ann Heng, Irem Cetin, Karim Lekadir, Oscar Camara, Miguel Angel Gonzalez Ballester, et al. Deep Learning Techniques for Automatic MRI Cardiac Multi-Structures Segmentation and Diagnosis: Is the Problem Solved? *IEEE Transactions on Medical Imaging*, 37(11):2514–2525, 2018. [2](#), [5](#)
- [5] Stella Biderman et al. Pythia: A Suite for Analyzing Large Language Models Across Training and Scaling. In *International Conference on Machine Learning*, pages 2397–2430. PMLR, 2023. [2](#)
- [6] Sijing Cai, Yunxian Tian, Harvey Lui, Haishan Zeng, Yi Wu, and Guannan Chen. Dense-UNet: a novel multiphoton in vivo cellular image segmentation model based on a convolutional neural network. *Quantitative Imaging in Medicine and Surgery*, 10(6), 2020. [2](#)
- [7] Hu Cao, Yueyue Wang, Joy Chen, Dongsheng Jiang, Xiaopeng Zhang, Qi Tian, and Manning Wang. Swin-Unet: Unet-Like Pure Transformer for Medical Image Segmentation. In *European Conference on Computer Vision*, pages 205–218. Springer, 2022. [1](#), [2](#), [5](#), [6](#), [7](#)
- [8] Jieneng Chen, Yongyi Lu, Qihang Yu, Xiangde Luo, Ehsan Adeli, Yan Wang, Le Lu, Alan Loddon Yuille, and Yuyin Zhou. TransUNet: Transformers Make Strong Encoders for Medical Image Segmentation. *ArXiv*, abs/2102.04306, 2021. [1](#), [2](#), [5](#), [6](#), [7](#)
- [9] Krzysztof Marcin Choromanski et al. Rethinking Attention with Performers. In *International Conference on Learning Representations*, 2021. [1](#), [2](#)
- [10] Foivos I. Diakogiannis, François Waldner, Peter Caccetta, and Chen Wu. ResUNet-a: A deep learning framework for semantic segmentation of remotely sensed data. *ISPRS Journal of Photogrammetry and Remote Sensing*, 162:94–114, 2020. [2](#)
- [11] Alexey Dosovitskiy and other. An Image is Worth 16x16 Words: Transformers for Image Recognition at Scale. *arXiv preprint arXiv:2010.11929*, 2020. [3](#)
- [12] Yunhe Gao, Mu Zhou, Di Liu, Zhennan Yan, Shaoting Zhang, and Dimitris N. Metaxas. A Data-scalable Transformer for Medical Image Segmentation: Architecture, Model Efficiency, and Benchmark, 2023. [1](#), [2](#)
- [13] Haifan Gong, Luoyao Kang, Yitao Wang, Xiang Wan, and Haofeng Li. nnmamba: 3d biomedical image segmentation, classification and landmark detection with state space model, 2024. [2](#)
- [14] Albert Gu and Tri Dao. Mamba: Linear-Time Sequence Modeling with Selective State Spaces, 2023. [1](#), [2](#), [3](#)
- [15] Albert Gu, Tri Dao, Stefano Ermon, Atri Rudra, and Christopher Ré. HiPPO: Recurrent Memory with Optimal Polynomial Projections. *Advances in Neural Information Processing Systems*, 33:1474–1487, 2020. [3](#)
- [16] Albert Gu, Karan Goel, and Christopher Ré. Efficiently Modeling Long Sequences with Structured State Spaces. *ArXiv*, abs/2111.00396, 2021. [1](#), [2](#)
- [17] Albert Gu, Isys Johnson, Karan Goel, Khaled Kamal Saab, Tri Dao, Atri Rudra, and Christopher Ré. Combining Recurrent, Convolutional, and Continuous-time Models with Linear State-Space Layers. *ArXiv*, abs/2110.13985, 2021. [2](#)
- [18] Ali Hatamizadeh et al. Swin UNETR: Swin Transformers for Semantic Segmentation of Brain Tumors in MRI Images. In *International MICCAI Brainlesion Workshop*, pages 272–284. Springer, 2022. [1](#), [2](#), [6](#), [7](#)
- [19] Ali Hatamizadeh et al. UNETR: Transformers for 3D Medical Image Segmentation. In *CVPR*, pages 574–584, 2022. [1](#), [2](#), [5](#), [6](#), [7](#)
- [20] Dan Hendrycks and Kevin Gimpel. Gaussian error linear units (gelus). *arXiv preprint arXiv:1606.08415*, 2016. [3](#)
- [21] Xiaohong Huang, Zhifang Deng, Dandan Li, and Xueguang Yuan. MISSFormer: An Effective Medical Image Segmentation Transformer. *arXiv preprint arXiv:2109.07162*, 2021. [6](#), [7](#)
- [22] Fabian Isensee, Paul F Jaeger, Simon AA Kohl, Jens Petersen, and Klaus H Maier-Hein. nnu-net: a self-configuring method for deep learning-based biomedical image segmentation. *Nature Methods*, 18(2):203–211, 2021. [2](#), [5](#), [6](#), [7](#)
- [23] Nikita Kitaev, Lukasz Kaiser, and Anselm Levskaya. Reformer: The Efficient Transformer. In *International Conference on Learning Representations*, 2020. [2](#)
- [24] Bennett Landman et al. Miccai multi-atlas labeling beyond the cranial vault—workshop and challenge. In *Multi-Atlas Labeling Beyond Cranial Vault—Workshop Challenge*, volume 5, page 12, 2015. [2](#), [5](#)
- [25] Y. Lecun, L. Bottou, Y. Bengio, and P. Haffner. Gradient-based learning applied to document recognition. *Proceedings of the IEEE*, 86(11):2278–2324, 1998. [1](#), [2](#)
- [26] Yue Liu, Yunjie Tian, Yuzhong Zhao, Hongtian Yu, Lingxi Xie, Yaowei Wang, Qixiang Ye, and Yunfan Liu. Vmamba: Visual state space model, 2024. [2](#)
- [27] Jun Ma, Feifei Li, and Bo Wang. U-mamba: Enhancing long-range dependency for biomedical image segmentation. *arXiv preprint arXiv:2401.04722*, 2024. [6](#), [7](#)

- [28] Lena Maier-Hein, Annika Reinke, Patrick Godau, Minu D Tizabi, Florian Buettner, Evangelia Christodoulou, Ben Glocker, Fabian Isensee, Jens Kleesiek, Michal Kozubek, et al. Metrics reloaded: Recommendations for image analysis validation. *Nature Methods*, pages 1–18, 2024. **5**
- [29] Fausto Milletari, Nassir Navab, and Seyed-Ahmad Ahmadi. V-Net: Fully Convolutional Neural Networks for Volumetric Medical Image Segmentation. In *2016 Fourth International Conference on 3D Vision (3DV)*, pages 565–571. IEEE, 2016. **2**
- [30] Michael Poli et al. Hyena Hierarchy: Towards Larger Convolutional Language Models. In *Proceedings of the 40th International Conference on Machine Learning, ICML’23*. JMLR.org, 2023. **2**
- [31] Olaf Ronneberger, Philipp Fischer, and Thomas Brox. U-Net: Convolutional Networks for Biomedical Image Segmentation. In *Medical Image Computing and Computer-Assisted Intervention – MICCAI 2015*. Springer, 2015. **1, 2, 3**
- [32] Saikat Roy, Gregor Koehler, Constantin Ulrich, Michael Baumgartner, Jens Petersen, Fabian Isensee, Paul F Jaeger, and Klaus H Maier-Hein. Mednext: transformer-driven scaling of convnets for medical image segmentation. In *International Conference on Medical Image Computing and Computer-Assisted Intervention*, pages 405–415. Springer, 2023. **5, 6, 7**
- [33] Jiacheng Ruan and Suncheng Xiang. Vm-unet: Vision mamba unet for medical image segmentation, 2024. **2**
- [34] Jo Schlemper, Ozan Oktay, Michiel Schaap, Mattias Heinrich, Bernhard Kainz, Ben Glocker, and Daniel Rueckert. Attention gated networks: Learning to leverage salient regions in medical images. *Medical Image Analysis*, 53:197–207, 2019. **1**
- [35] Abdelrahman M Shaker, Muhammad Maaz, Hanoona Rasheed, Salman Khan, Ming-Hsuan Yang, and Fahad Shahbaz Khan. Unetr++: delving into efficient and accurate 3d medical image segmentation. *IEEE Transactions on Medical Imaging*, 2024. **5**
- [36] Ashish Vaswani, Noam Shazeer, Niki Parmar, Jakob Uszkoreit, Llion Jones, Aidan N Gomez, Łukasz Kaiser, and Illia Polosukhin. Attention is all you need. *Advances in neural information processing systems*, 30, 2017. **1, 2**
- [37] Ben Wang and Aran Komatsuzaki. GPT-J-6B: A 6 Billion Parameter Autoregressive Language Model. <https://github.com/kingoflolz/mesh-transformer-jax>, May 2021. **2**
- [38] Sinong Wang, Belinda Z. Li, Madian Khabsa, Han Fang, and Hao Ma. Linformer: Self-Attention with Linear Complexity. *ArXiv*, abs/2006.04768, 2020. **1, 2**
- [39] Wenxuan Wang, Chen Chen, Meng Ding, Hong Yu, Sen Zha, and Jiangyun Li. TransBTS: Multimodal Brain Tumor Segmentation Using Transformer. In *Medical Image Computing and Computer Assisted Intervention–MICCAI 2021*, pages 109–119. Springer, 2021. **5, 6, 7**
- [40] Ziyang Wang, Jian-Qing Zheng, Yichi Zhang, Ge Cui, and Lei Li. Mamba-unet: Unet-like pure visual mamba for medical image segmentation, 2024. **2**
- [41] Yutong Xie et al. CoTr: Efficiently Bridging CNN and Transformer for 3D Medical Image Segmentation. In *Medical Image Computing and Computer Assisted Intervention*, pages 171–180. Springer, 2021. **5, 6, 7**
- [42] Zhaohu Xing, Tian Ye, Yijun Yang, Guang Liu, and Lei Zhu. SegMamba: Long-range Sequential Modeling Mamba For 3D Medical Image Segmentation. *arXiv preprint arXiv:2401.13560*, 2024. **2**
- [43] Guoping Xu, Xuan Zhang, Xinwei He, and Xinglong Wu. LeViT-UNet: Make Faster Encoders with Transformer for Medical Image Segmentation. In *Chinese Conference on Pattern Recognition and Computer Vision (PRCV)*, pages 42–53. Springer, 2023. **5, 6, 7**
- [44] Hanwei Zhang, Ying Zhu, Dan Wang, Lijun Zhang, Tianxiang Chen, Ziyang Wang, and Zi Ye. A Survey on Visual Mamba. *Applied Sciences*, 14(13):5683, 2024. **2**
- [45] Susan Zhang et al. Opt: Open pre-trained transformer language models. *arXiv preprint arXiv:2205.01068*, 2022. **2**
- [46] Hong-Yu Zhou, Jiansen Guo, Yinghao Zhang, Xiaoguang Han, Lequan Yu, Liansheng Wang, and Yizhou Yu. nnFormer: Volumetric Medical Image Segmentation via a 3D Transformer. *IEEE Transactions on Image Processing*, 2023. **5, 6, 7**